IOP Publishing Journal of Physics: Condensed Matter

J. Phys.: Condens. Matter **28** (2016) 036001 (10pp) doi:10.1088/0953-8984/28/3/036001

The low-temperature magnetostructure and magnetic field response of $Pr_{0.9}Ca_{0.1}MnO_3$: the roles of Pr spins and magnetic phase separation

J Tikkanen[1], M Geilhufe[2], M Frontzek[3], W Hergert[4], A Ernst[2], P Paturi[1] and L Udby[5]

[1] Wihuri Physical Laboratory, Dept. of Physics and Astronomy, University of Turku, FI-20014 Turku, Finland
[2] Theory Department, Max Planck Institute of Microstructure Physics, D-06120 Halle, Germany
[3] Laboratory for Neutron Scattering, Paul Scherrer Institute, CH-5232 Villigen PSI, Switzerland
[4] Naturwissenschaftliche Fakultät II, Institut für Physik, Martin-Luther-Universität Halle-Wittenberg, D-06099 Halle, Germany
[5] X-Ray and Neutron Science, Niels Bohr Institute, University of Copenhagen, DK-2100 Copenhagen, Denmark

E-mail: jussi.tikkanen@utu.fi

Received 5 October 2015, revised 25 November 2015
Accepted for publication 2 December 2015
Published 6 January 2016

Abstract

With the goal of elucidating the background of photoinduced ferromagnetism phenomena observed in the perovskite structured (Pr,Ca) manganites, the low-temperature magnetostructure of the material $Pr_{0.9}Ca_{0.1}MnO_3$ was revised using cold neutron powder diffraction, SQUID magnetometry and *ab initio* calculations. Particular emphasis was placed on determining the presence of nanoscale magnetic phase separation. Previously published results of a canted A-AFM average ground state were reproduced to a good precision both experimentally and theoretically, and complemented by investigating the effects of an applied magnetic field of 2.7 T on the magnetostructure. Explicit evidence of nanoscale magnetic clusters in the material was obtained based on high-resolution neutron diffractograms. Along with several supporting arguments, we present this finding as a justification for extending the nanoscale magnetic phase separation model of manganites to the material under discussion despite its very low Ca doping level in the context of the model. In the light of the new data, we also conclude that the low temperature magnetic moment of Pr must be ca. 300% larger than previously thought in this material, close to the high spin value of 2 μ_B per formula unit.

Keywords: manganite, magnetic, structure, nanoscale, phase, separation

(Some figures may appear in colour only in the online journal)

1. Introduction

The perovskite manganite family $Pr_{1-x}Ca_xMnO_3$ (PCMO), i.e. the set of solid solutions between $PrMnO_3$ and $CaMnO_3$, contains a variety of multifunctional semiconductor materials. Since the first description of the magnetic and nuclear structure of PCMO based on neutron diffraction (ND) by Jirák *et al* in 1985 [1], the colossal resistivity switching and related electromagnetic phase separation behaviour of PCMO (which can be observed under the influence of many different external stimuli such as pressure, electric and magnetic fields and electromagnetic radiation [2–9]) has sparked numerous fascinating investigations. In particular, a very recent study [10] has shown the capacity of a magnetically biased PCMO thin film

to perform as a light-activated electronic switch with an off/on resistivity ratio higher than 10^7thanks to the dynamically adjustable equilibrium between insulating antiferromagnetic (AFM) regions and metallic ferromagnetic (FM) clusters.

Previous ND studies of PCMO have explored the prominent Jahn–Teller distortion at $x = 0.0$ [11], the exotic FM insulator state at $x = 0.25$ [12], the electronic phase separation caused by the dominant double exchange (DE) interaction at $0.2 \leqslant x \leqslant 0.33$ [13–15], photoinduced magnetism [8] and the first order metamagnetic transition [5] at $x = 0.3$, the effect of Sr doping at $x = 0.4$ [16] and the complex relations between charge and spin ordering around $x = 0.5$ [17–20].

There have been some objections [21] to the validity of the DE-driven electromagnetic cluster phase separation framework in the case of PCMO [3, 8], but nearly all published results are compatible with the phase separation scheme. The motivation for our present work was to explicitly clarify the situation for PCMO at the Ca doping level $x = 0.1$, which is outside the 'optimal' doping range for the colossal resistivity phenomena, but has still been recently associated with a related, DE-driven persistent photoinduced magnetization phenomenon [7]. Another incentive for our inquiry came from the observation that even though the published magnetization isotherms [22] and AC magnetic susceptibility data [23] are entirely compatible with a 'simple' canted antiferromagnet model [1, 24] at $x = 0.1$, one only has to go up to $x = 0.2$ to find strong signs of magnetic cluster glass behaviour [23] and to $x = 0.3$ to conclusively observe a metamagnetic insulator-to-metal transition (IMT) [3, 8, 22] with a critical magnetic field of order $\mu_0 H_c \approx 5$ T [22]. Both the cluster glass behaviour and the IMT are understood to originate from shifts in a dynamic AFM–FM phase equilibrium [3].

We now report a revision of the published ground state magnetostructure of PCMO $x = 0.1$ [1, 24] based on a combination of data from cold neutron powder diffractometry, SQUID magnetometry and *ab initio* calculations. Thanks to the high resolution of our experiments, the possibility of performing ND in a relatively strong external magnetic field, and the development of powerful computational methods, we are able to suggest a refinement of the magnetic ground state, and reassess the roles of Pr spins and the electromagnetic phase separation in PCMO $x = 0.1$.

2. Materials and methods

A $Pr_{0.9}Ca_{0.1}MnO_3$ sample (PCMO $x = 0.1$) was produced by the following route, which we may generally recommend for PCMO. Powders of analysis grade Pr_6O_{11}, $CaCO_3$ and Mn_2O_3 were dried overnight at 470 K. Stoichiometric amounts were weighed on an analytical balance and mixed by mortaring. The mixture was calcined in air at 1020 K for 60 h. This temperature is high enough to readily calcine $CaCO_3$ into CaO, but still low enough to avoid the spontaneous reduction of Mn_2O_3 into Mn_3O_4, a common persistent impurity phase in manganites. Finally, the calcined oxide mixture was repeatedly mortared and sintered in air at 1600 K for 36 h at a time. Room temperature powder x-ray diffraction (XRD) was used to monitor the formation and purity of the PCMO phase. Two sintering burns were found sufficient for obtaining a pure, well crystallized sample. Using the XRD data and later ND results to determine the cation and oxygen stoichiometries, respectively, the chemical composition of the sample was found to be $Pr^{3+}_{0.90(1)}Ca^{2+}_{0.10(1)}Mn^{3+}_{0.88(3)}Mn^{4+}_{0.12(3)}O^{2-}_{3.01(1)}$. The subscripts in parentheses indicate the standard deviations obtained via Rietveld refinement.

Powder ND experiments were performed on the DMC instrument at SINQ, Paul Scherrer Institute, Switzerland. The polycrystalline PCMO was pelletized and suspended in a ventilated Al sample holder by a Cd spacer wrapped in Al foil. This assembly was to prevent the reorientation of crystallites when an external magnetic field was applied. Diffractograms were collected at the temperatures $T = 160$ K, 125 K, 90 K, 55 K and 5 K using the wavelength $\lambda \approx 2.45$ Å, and in high resolution at $T = 160$ K, 55 K and 5 K using $\lambda \approx 4.20$ Å. A version of each diffractogram was first collected without an external magnetic field and then in a field of 2.7 T (upper hardware limit minus a 0.1 T safety margin), with the sample degaussed in the paramagnetic (PM) state at 160 K and field cooled whenever appropriate. The ND data were analyzed using Levenberg–Marquardt, Le Bail and finally Rietveld fits provided by the FullPROF program package [25]. The nuclear structural analysis was performed in the space group *Pbnm*. The propagation vector (0, 0, 0) was assumed for all magnetic structures, providing simplicity and sufficient accuracy. The absence of any preferred crystallite orientation, initial or magnetically induced, was confirmed by Rietveld fits to the $T = 160$ K, PM state datasets (the sample was put through all in-field measurements at 2.45 Å before the 4.20 Å, 160 K data were collected).

The temperature dependence of the magnetization of PCMO $x = 0.1$ was measured in magnetizing fields of $\mu_0 H = 2.7$ T (same as the ND experiment) and $\mu_0 H = 4.8$ T (hardware limit) using a Quantum Design MPMS XL SQUID open-circuit magnetometer. The powder sample was rolled into a ball of PTFE tape, fixing the demagnetizing factor at $N \approx 1/3$. The validity of this N value for calculations was verified by measuring a demagnetizing curve in the soft ferromagetic state at $T = 70$ K.

Next to the experimental studies of the material an *ab initio* investigation of $PrMnO_3$ and $Pr_{0.9}Ca_{0.1}MnO_3$ was performed by means of the multiple-scattering Korringa–Kohn–Rostocker Green function method (KKR) [26], which is based on density functional theory (DFT) [27, 28]. We used a scalar-relativistic approach [29, 30] as it is implemented within the computer program Hutsepot. The evaluation of the Green function in terms of spherical harmonics was expanded up to a maximal angular momentum of $l = 3$. As an approximation for the exchange-correlation functional we used the LibXC implementation [31] of PBE–Sol [32], which is a generalized gradient approximation specialised for solids and surfaces. To properly simulate the $Pr_{0.9}Ca_{0.1}MnO_3$ compound and to include oxygen vacancies the coherent-potential approximation (CPA) [33–35] was applied. Correlation effects of localized Mn *d*- and Pr *f*-electrons were treated by using a DFT + U approach

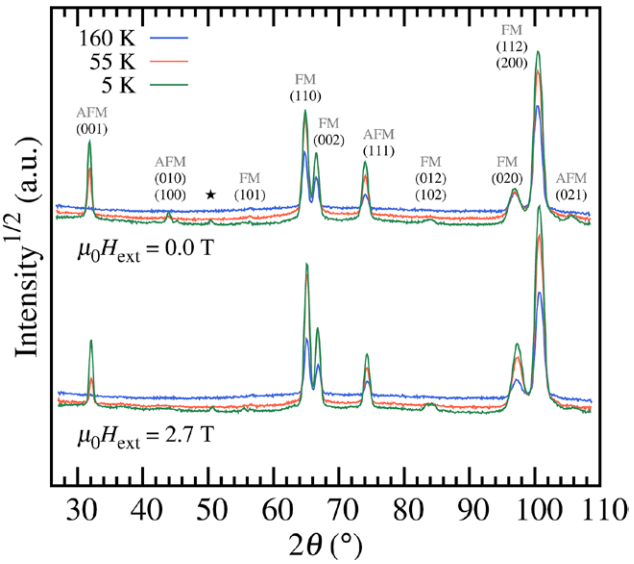

Figure 1. Observed high-resolution neutron diffractograms at the wavelength $\lambda = 4.20$ Å. The peaks are indexed corresponding to the space group *Pbnm*. They are also labeled FM or AFM based on the predominant type of magnetic order associated with them, although many have contributions from both FM and AFM order. The star symbol marks a magnetic peak associated with the (1 0 1) reflection of an otherwise undetected Mn_3O_4 impurity phase.

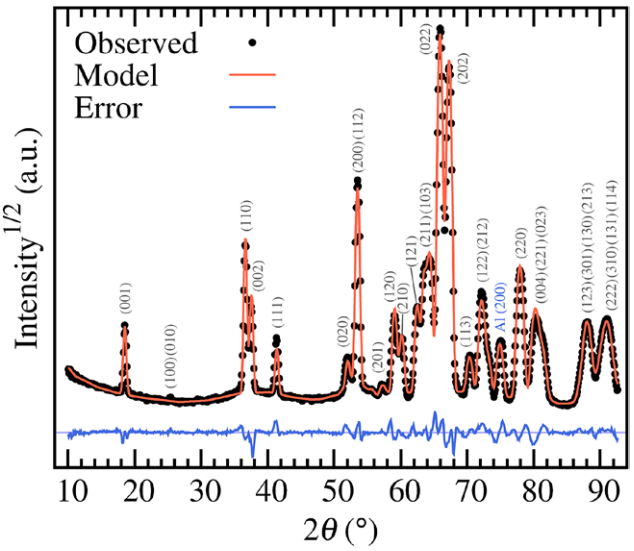

Figure 2. The Rietveld refinement of the $\lambda = 2.45$ Å neutron diffraction dataset at $T = 55$ K, $\mu_0 H = 0.0$ T. The PCMO peaks have been indexed in correspondence with the space group *Pbnm*. The observed and calculated intensities are drawn on a square-root scale, which somewhat emphasizes features that have small absolute intensities. The error curve shows the direct visual difference between the two intensity plots.

[36] with values $U_d^{\text{eff}} = U_d - J = 1$ eV and $U_f^{\text{eff}} = U_f - J = 3$ eV, respectively. The magnetic ordering observed during the experiments was cross-checked by calculating Heisenberg exchange parameters J_{ij} within the framework of the magnetic force theorem [37] and by applying a Monte Carlo method.

3. Results

Figure 1 shows a summary of the raw $\lambda = 4.20$ Å high resolution neutron diffractograms at the temperatures $T = 160$ K (PM state), $T = 55$ K and $T = 5$ K (AFM state), both with and without an external magnetic field of $\mu_0 H = 2.7$ T. The datasets at different $\mu_0 H$ are separated by an arbitrary intensity shift, but for each applied field the increase of the background with temperature is due to incoherent scattering from PM ions. The PCMO $x = 0.1$ reflections are indexed with respect to the *Pbnm* unit cell. The predominant magnetic character (FM or AFM) of each peak is also indicated, although many peaks like (1 1 1) actually have both FM and AFM intensity contributions based on the underlying magnetostructural symmetry conditions. Note how the increased background cancels the temperature dependence of the FM (0 2 0) reflection at $\mu_0 H = 0.0$ T. A very small amount of Mn_3O_4, a typical ferrimagnetic impurity phase in manganites [38–41] with a Néel transition at $T_N \approx 45$ K [42], can be observed in the 5 K diffractograms due to the considerably low noise level (high counting time). No other signs of complications from this impurity were met during the course of the present work.

A typical Rietveld plot is given in figure 2, showing the refinement of the dataset at $\lambda = 2.45$ Å, $T = 55$ K, $\mu_0 H = 0.0$ T. Thanks to the smaller λ, a greater range of PCMO $x = 0.1$ reflections are obtained—they are again indexed within the *Pbnm* unit cell. A single peak from the Al sample holder is also visible. As can be seen from the error curve, the noise level is very low, indicating excellent counting statistics, even overcounting. The majority of the residual error is due to imperfect peak shape modeling; $\chi^2 = 26.18$ for this Rietveld fit, whereas $\chi^2 = 25.70$ for the corresponding Le Bail fit. Therefore, the excess contribution [43] to χ^2 from the structural and magnetic models is only a rather acceptable 0.48. The peak shape modeling problem is fundamentally due to strongly nonlinear upturns of the background around magnetic peaks, a phenomenon arguably resulting from diffraction from

Table 1. Parameters of the PCMO nuclear lattice in the PM state ($T = 160$ K).

$T = 160$ K, $\mu_0 H = 0.0$ T			
Cell		a	5.4321(3) Å
		b	5.5850(3) Å
		c	7.6061(4) Å
Mn	(4b)	x	1/2
		y	0
		z	0
Pr, Ca	(4c)	x	−0.009(1)
		y	0.040(1)
		z	1/4
O_1	(4c)	x	0.0825(8)
		y	0.4873(8)
		z	1/4
O_2	(8d)	x	−0.2833(5)
		y	0.2995(4)
		z	0.0384(4)

Note: The numbers in parentheses indicate the standard deviations of the least significant digits of the respective parameter values. Except for a, b and c, the changes to the parameters were negligible at lower temperatures.

Table 2. Experimental AFM-state magnetostructural parameters of PCMO $x = 0.1$: the lattice paramters a, b, c of the *Pbnm* cell, the orientations ϕ_1, ϕ_2 of the FM Mn spin layers (defined as angles from the x axis by the right hand rule around z) and the Mn and Pr magnetic moments, m_{Mn} and m_{Pr}, per formula unit.

		$\mu_0 H = 0.0$ T	$\mu_0 H = 2.7$ T
$T = 55$ K	a (Å)	5.4329(3)	5.4353(3)
	b (Å)	5.5836(3)	5.5848(3)
	c (Å)	7.6076(4)	7.6135(4)
	ϕ_1 (°)	53(5)	73(5)
	ϕ_2 (°)	102(5)	106(5)
	m_{Mn} (μ_B)	2.74(4)	2.79(9)
	m_{Pr} (μ_B)	1.0(2)	1.5(3)
$T = 5$ K	a (Å)	5.4337(2)	5.4353(2)
	b (Å)	5.5790(2)	5.5799(2)
	c (Å)	7.6080(3)	7.6126(3)
	ϕ_1 (°)	28(5)	45(5)
	ϕ_2 (°)	91(5)	92(5)
	m_{Mn} (μ_B)	3.41(8)	3.56(9)
	m_{Pr} (μ_B)	1.8	1.8

Note: The numbers in parentheses indicate the standard deviations of the least significant digits of the respective parameter values. To overcome a texturing issue of the magnetic diffraction domains (see section 3.1), the Pr moments were not refined at $T = 5$ K, but fixed at the full high-spin value suggested by calculations and SQUID magnetometry (section 3.2).

a distribution of nanoscale and mesoscale domains (diameter $d < 500$ nm) [44]. This matter will be discussed in more depth in sections 3.2 and 4.

The PCMO $x = 0.1$ structural model obtained from the $\lambda = 2.45$ Å, $T = 160$ K PM state diffractogram is summarized in table 1. This model was used as a basis for all magnetic Rietveld models, only the cell parameters a, b and c were refined separately for each dataset using Le Bail fits. Due to the low neutron wavelength and the resulting limited peak-to-peak resolution, the structural data of previous reports could not be improved upon [1, 22].

3.1. Zero-field magnetostructure

The experimentally obtained average low-temperature magnetostructure of PCMO $x = 0.1$ is summarized in table 2 and visualized in figure 3. The overall results are in good agreement with previous studies. A very wide PM–FM transition takes place in the temperature interval from $T = 130$ K to $T = 80$ K [22, 23], below which a transition to an A-type AFM ground state takes place at $T \approx 70$ K [1, 23, 24]. A very small G-AFM component along [0 0 1], probably due to a weak intrinsic Dzyaloshinskii–Moriya interaction [2], is indicated by the presence of the peak group (1 0 0)(0 1 0) at $T = 5$ K, but omitted in the construction of figure 3 and table 2. The total ordered Mn magnetic moment at 5 K in the absence of an external magnetic field was determined to be 3.41 ± 0.08 μ_B Mn^{-1} (Bohr magnetons per Mn ion). It is consistent with to the value of 3.35 μ_B Mn^{-1}, which was reported by Jirák *et al* [1]. The calculated value of 3.61 μ_B Mn^{-1} is slightly higher.

The magnetocrystalline FM easy axis is [0 1 0] at and above $T = 55$ K and turns towards [1 1 0] at lower temperatures as reported [1]. However, our ND data indicate that the average angle of the Mn moments does not fall below $60° \pm 10°$ from the a axis even at $T = 5$ *K*. As reported before [1], the Pr mangetic moments were found to be partially ordered already at 55 K and determined to be oriented along the FM component of the Mn moments. Technically, the Pr moments were fixed parallel to this direction in the final Rietveld refinement.

In contrast, the magnitude of the Pr moment was seen to considerably exceed the previously proposed value of ca. 0.50 μ_B per ion, being closer to 1 μ_B per ion at 55 K and 2 μ_B per ion at 5 K (this point will be elaborated on in section 3.2), but could not be quantified accurately by ND data alone due to a texturing phenomenon of the magnetic diffraction intensity. To technically overcome this issue, all of the preferred orientation was attributed to an additional magnetic Pr phase in the Rietveld model, sacrificing the accuracy of the Pr FM moment, but retaining a realistic [1] best estimate of the Mn FM moment (2.95 ± 0.09 μ_B Mn^{-1} at $T = 5$ K) along with the total moment (table 2). The texturing effect, observed as an excess of magnetic intensity in the (1 1 2)(2 0 0) peak group compared with all other magnetic peaks, was attributed to the coercivity of PCMO [22] which allows coherent magnetization to preferably occur in crystallites which have their easy axis along the external magnetic field. The occurrence of this effect even in supposed zero-field conditions is a sign of the instrument magnet being incompletely degaussed; indeed no specific steps were taken to degauss the magnet. The mechanical reorientation of crystallites due to the applied magnetic field could be ruled out as stated in section 2.

As our *ab initio* results confirm, in the A-AFM state of PCMO $x = 0.1$ the Mn spins form FM (0 0 1) planes, which are AFM coupled, but can be pictured to counterrorate around the lattice vector **c** to give a net FM moment. The calculations give large values of Heisenberg exchange parameters in plane, $J_{Mn_1 Mn_2} \approx 8.4$ meV, confirming the ferromagnetic coupling (see figure 4). A negative value of the Heisenberg exchange parameter ($J_{Mn1Mn3} \approx -1.1$ meV) is observed for the coupling between manganese atoms along the cell diagonal. Due to the crystal symmetry, this coupling occurs 8 times and causes the antiferromagnetic structure. However, the system is very sensitive regarding structural perturbations or impurities, which might explain the proposed presence of purely ferromagnetic domains within PCMO $x = 0.1$ [7]. It must be kept in mind when looking at figure 3 that the ND-derived model only reflects the average magnetostructure, which might in reality be a combination of relatively undistorted FM and A-AFM clusters [3, 7].

The calculated density of states (DOS) for $Pr_{0.9}Ca_{0.1}MnO_3$ is illustrated in figure 5. By doping $PrMnO_3$ with calcium the Fermi energy is shifted towards the valence band and the model system becomes metallic, which does not agree with experimental data indicating semiconductivity [45]. A metallic behaviour of the material also leads to positive Heisenberg exchange parameters J_{ij} and therefore to a ferromagnetic structure (dashed line). However, very small concentrations of impurities or oxygen vacancies are likely [46]. By using CPA and introducing 2% of oxygen vacancies the Fermi energy is shifted back towards the conduction band and a realistic semiconducting behaviour can be reproduced, along with the

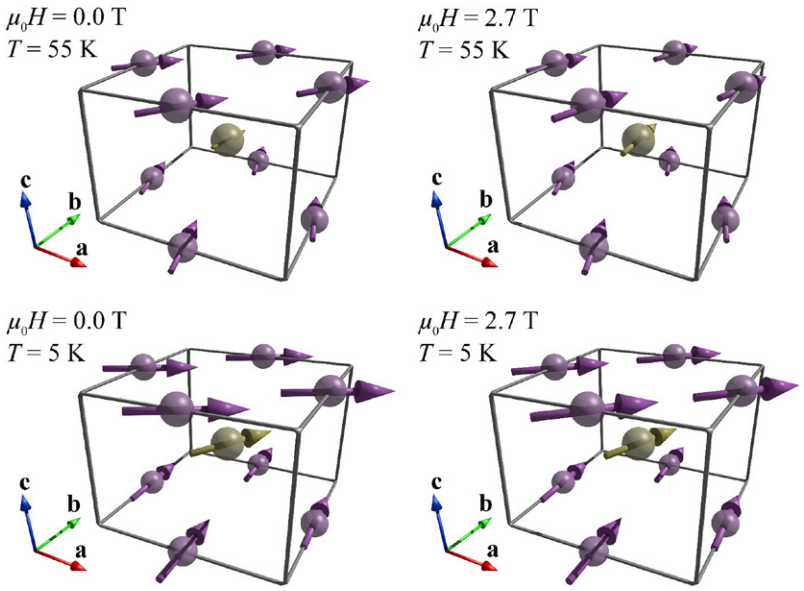

Figure 3. Real space illustrations of the average magnetic structures experimentally found in PCMO $x = 0.1$ by ND. For clarity, oxygen atoms are omitted and only a half of the magnetic unit cell is shown along z. The indicated coordinate axes correspond to those of the *Pbnm* unit cell. The arrows on the edges of the drawn cells represent Mn magnetic moments (colour online: purple), the ones in the middle stand for the Pr moment (colour online: yellow). The scaling of the arrows reflects the relative magnitudes of the magnetic moments (table 2), but Mn moment mangitudes are not directly visually comparable to Pr due to the use of a different scaling factor for each element.

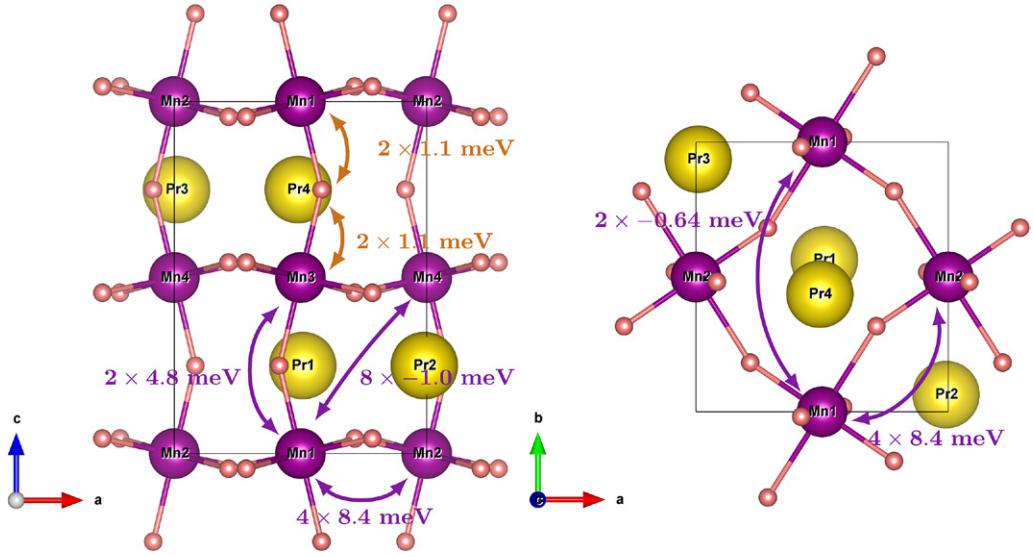

Figure 4. The calculated Heisenberg exchange parameters J_{ij} among Mn and Pr ions within the unit cell of PCMO $x = 0.1$. The small unlabeled spheres represent oxygen.

experimentally verified A-AFM structure. Although such a vacancy concentration is probably unrealistically high [46], the results highlight the importance of considering structural defects when modeling manganites.

3.2. Response to magnetic field

As reflected by figure 3 and table 2, the ND data collected in the external magnetic field of $\mu_0H = 2.7$ T can be explained within the same canted A-AFM model framework, which was applied at $\mu_0H = 0.0$ T. In particular, this average structure model gives a straightforward interpretation of the observation that applying the magnetic field effectively shifted some ND intensity from the predominantly AFM-related peaks, like (0 0 1), to the FM ones, like (0 2 0). Figure 6 gives a quantitative account of this phenomenon in terms of relative peak intensity changes, $(I_H - I_0)/I_0$, caused by the external magnetic field. The FM (0 0 1) spin sublattices simply rotate around c towards the prevailing magnetocrystalline easy axis ([0 1 0] at $T = 55$ K, closer to [1 1 0] at $T = 5$ *K*) in response to the applied field, thus enhancing the FM component while suppressing the AFM component at low temperatures. The process was found to be reversible within the resolution of the experiments; the original zero-field magnetostructure was recovered as soon as the field was switched off.

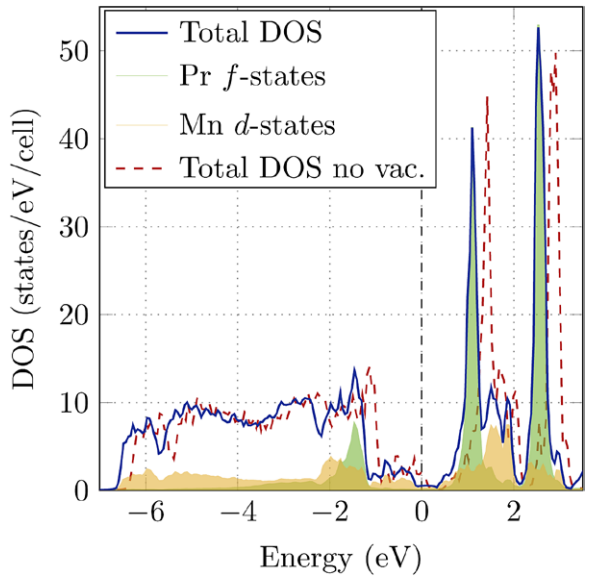

Figure 5. The calculated electronic density of states (DOS) of PCMO $x = 0.1$ with 2% (hypothetical) oxygen vacancies. The Fermi energy at 0 eV is effectively surrounded by a band gap. The contributions from the magnetic Pr 4*f*-states and Mn 3*d*-states are highlighted, and a calculated total DOS in the absence of oxygen vacancies (dashed line) is also given for comparison.

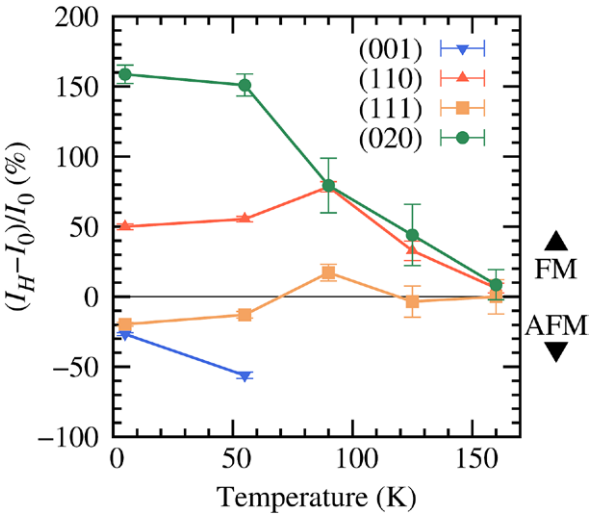

Figure 6. Observed relative changes in the intensities of the major magnetic neutron diffraction peaks of PCMO upon the application of the external magnetic field, $\mu_0 H = 2.7$ T. FM-dominated peaks have a positive ratio of $(I_H - I_0)/I_0$. This ratio is negative for AFM-dominated peaks. The plot is based on single peak Levenberg–Marquardt least squares fits [47] to the $\lambda = 2.45$ Å data. The error bars span the sum of the standard deviations of the two fits used to construct each point.

The total magnetic moments of Mn and Pr remained constant within error limits when the field was applied, although subtle increases in the Mn and Pr moments appear to be indicated by the best-fit values. This would be a natural consequence of reducing the amount of domain walls where the magnetization is incoherent. The actual magnetization is known [22] to vary more versus the applied field than the sums of the moments in table 2, this is due to the reorientation of existing magnetic domains. Magnetostrictive cell volume

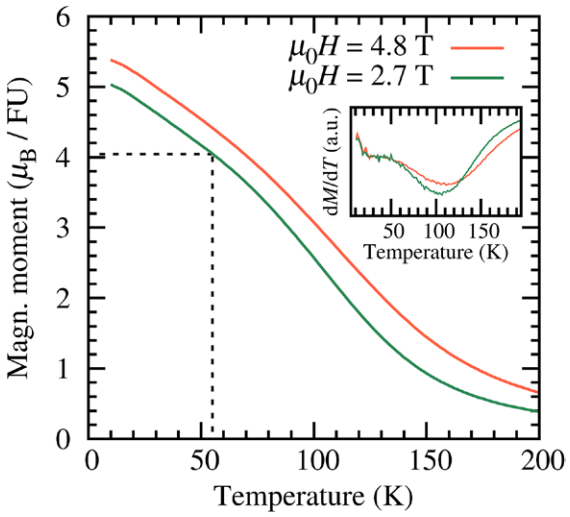

Figure 7. The temperature dependence of the molar magnetization of PCMO, in Bohr magnetons (μ_B) per the formula unit $Pr_{0.9}Ca_{0.1}MnO_3$ (FU), based on SQUID magnetometry. The two solid lines correspond to magnetic moments measured at the different magnetizing fields, $\mu_0 H$, indicated in the legend. The black dashes point out the approximate total FM moment expected in our ND measurements at $T = 55$ K. The line widths exceed the random instrument errors, but systematical scaling errors of 5% may be present in the moments due to the imperfectly known demagnetizing field. The inset shows the derivatives of the two curves, there the random noise can be estimated visually.

increases of 0.14% and 0.11% were observed at 55 K and 5 K, respectively, when the field was engaged. The magnetostriction was somewhat anisotropic, being strongest along [0 0 1] (table 2).

Compared with a previous report of the Pr magnetic moment, estimated at $0.50 \pm 0.03\,\mu_B$ per Pr^{3+} ion at $T = 4.2$ K [1], our ND results show a much larger contribution from Pr. To clarify the matter, we measured the temperature dependence of the magnetization of PCMO $x = 0.1$ using a SQUID magnetometer (figure 7). It is beyond doubt that the total magnetic moment exceeds the reported [1] value of $3.35 + 0.45 = 3.80\,\mu_B$ per formula unit, and since the absolute maximum contribution from high-spin Mn^{3+} is 3.8 μ_B per formula unit, we propose to assume the full high-spin value of 2 μ_B per Pr ion to explain the ND data and the SQUID-determined low-temperature moment of 5.4 ± 0.3 μ_B per formula unit. Our *ab initio* studies support this claim, with calculated Mn moments of 3.61 μ_B and, indeed, Pr moments of 2.00 μ_B per ion.

Unfortunately the temperature dependence of the ordered Pr magnetic moment could not be addressed rigorously by experimental means. It was problematic to isolate the contribution of Pr to the magnetic ND intensity, in addition to which the ND measurements were only performed at very few different temperatures in order to afford better counting statistics for each diffractogram. Since the SQUID data (figure 7) also showed no clear signs of a separate Pr transition, we proceeded to investigate the matter computationally. The calculated Heisenberg exchange parameters showed that there is no exchange coupling between Pr atoms but a ferromagnetic coupling (about 1 meV) between Mn and Pr. This suggests that there is no ordering of Pr moments before the ordering of

Table 3. The effect of the external magnetic field on the full-width-at-half-maximum, W, and the Gaussianity, η, of the AFM ND peak (0 0 1) and the FM ND peaks (1 1 0) and (0 0 2) ($\lambda \approx 4.20$ Å data) at different temperatures.

	(hkl)	W_0 (°)	W_H (°)	η_0	η_H
$T = 160$ K	(0 0 1)	—	—	—	—
	(1 1 0)	0.761(5)	—	0.27(7)	—
	(0 0 2)	0.720(9)	—	0.30(7)	—
$T = 55$ K	(0 0 1)	0.564(5)	0.541(8)	0.18(3)	0.13(5)
	(1 1 0)	0.803(3)	0.755(2)	0.35(7)	0.21(8)
	(0 0 2)	0.784(5)	0.723(4)	0.34(7)	0.21(8)
$T = 5$ K	(0 0 1)	0.590(3)	0.541(9)	0.24(2)	0.15(5)
	(1 1 0)	0.831(3)	0.756(2)	0.25(8)	0.21(6)
	(0 0 2)	0.807(5)	0.724(4)	0.33(8)	0.19(6)

Note: The (0 0 1) superstructure peak is absent in the PM state at 160 K. The lower indices 0 and H respectively indicate the absence and presence of the 2.7 T external magnetic field. The numbers in parentheses indicate the standard deviations of the least significant digits of the respective parameter values.

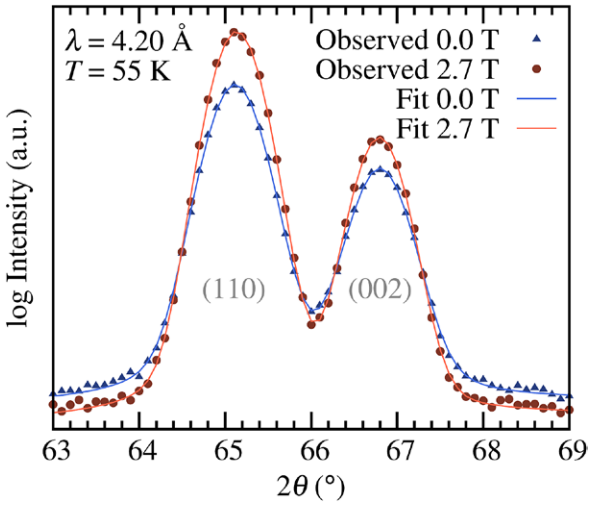

Figure 8. The effect of the applied magnetic field on the shapes of the ND peaks (1 1 0) and (0 0 2). The experimental ND datasets at $T = 55$ K, $\lambda = 4.20$ Å are shown along with the respective pseudo-Voigt sum profiles obtained by Levenberg–Marquardt [47] fits. The semilogarithmic scale strongly emphasizes low-intensity features.

Mn moments occurs. By performing Monte Carlo simulations with an applied magnetic field, we found that the Pr moments order simultaneously with the Mn moments, which indeed explains the shape of the transition seen in figure 7.

The shapes of the first three magnetic ND peaks at low 2θ (figure 1), where the magnetic intensity resolution is at its best, were analyzed in detail by fitting individual pseudo-Voigt profiles to the $\lambda = 4.20$ Å data using the Levenberg–Marquardt least-squares algorithm [47] as provided by FullPROF [25]. Table 3 lists the extracted full-width-at-half-maximum parameters, W_i, and Gaussianities, η_i ($\eta_i = 0$ for completely Gaussian and $\eta_i = 1$ for completely Lorentzian profile functions). There was a surprisingly strong reduction in W_i and a trend towards Gaussianity when the magnetic field was applied. Figure 8 shows an example fit over the reflections (1 1 0) and (0 0 2) at $T = 55$ K. In addition to increasing the overall FM ND intensity, the applied field significantly decreased the background level around the peak group. This was reflected by the decrease of the Lorentzian component in the obtained pseudo-Voigt profiles. The origin of the Lorentzian background will be modeled and discussed in section 4 in terms of nanoscale magnetic domains.

Comparing the PM-state data at $T = 160$ K against those recorded at 55 K and 5 K, below the Néel temperature, it is clear that there was excess diffraction line broadening due to the magnetic diffraction domains. With a rough knowledge of the instrumental linewidth of the DMC, we could employ Scherrer's equation [44] $d = k\lambda/\beta\cos\theta$ to make order-of-magnitude estimates of diffraction domain sizes. Here d is the average crystallite diameter, $k \approx 1$ a shape constant, λ the wavelength of the incident (neutron) radiation, $\beta = \Delta(2\theta)$ the FWHM of the diffraction peak (in radians) minus the instrumental linewidth, and θ the Bragg diffraction angle. Based on the assumption of round diffraction domains ($k = 0.9$ [44]) and the peak width values W_i extracted from table 3, the average diffraction domain size grew from $d \approx 300$ nm to $d \approx 1000$ nm when the field was applied at $T = 5$ K.

4. Discussion

In short, the goal of our present study was to elucidate whether it is physically more sensible to model the ground state of PCMO $x = 0.1$ as a canted A-type antiferromagnet [1, 24] or as a dynamic mixture of pure FM and A-AFM phases [7, 23]. We presented a rather accurate reproduction of the previously published canted A-AFM model and successfully extended it to also explain the response of PCMO to an external magnetic field. Considering the elegance and descriptive power of this simple model, one should be rather conservative when considering alternative explanations for the experimental observations.

To distinguish a canted AFM structure from a FM-AFM phase separation by means of a Rietveld analysis is problematic since various interpretations of the data are conceivable. E.g. the spin structures in table 2 and figure 3 could indicate a superposition of pure A-AFM and FM phases, with approximately 60% of Mn ions ordered in a FM pattern at $T = 5$ K and no applied magnetic field. In fact, this kind of superposition is roughly how the numerical Rietveld model was constructed.

The observed positive volumetric magnetostriction values (0.14% at 55 K and 0.11% at 5 K) are considerably high. Nonetheless, such values have also been reported in the past for materials where $3d$ and $4f$ transition metals are mixed [48]. The magnetic anisotropy energy function becomes rather complicated when $4f$ orbitals are involved, so the source of this magnetostriction is not easily modeled. Superficially similar magnetostriction phenomena have been associated with changes in the phase FM-AFM equilibrium in PCMO [49] and related manganites [50] at alkaline earth dopant concentrations near $x = 0.5$ (the specific volume of the FM phase is larger due to disorder). However, at these concentrations, the presence of FM-AFM phase separation has been established by other means [6, 8, 10], and extending the cluster phase separation description down to $x = 0.1$ for PCMO on the basis of magnetostriction is not a valid implication.

The strongest argument for the presence of a cluster phase separation situation in PCMO $x = 0.1$ is provided by the magnetic broadening observed in the high-resolution $\lambda = 4.20$ Å neutron diffractograms. Whereas the estimated magnetic diffraction domain growth from 300 nm to 1000 nm upon the application of the external magnetic field can be a natural consequence of the merging of domains, the prominent Lorentzian tails (figure 8) were unexpected. Like most neutron powder diffractometers, the DMC is known to have a practically Gaussian instrumental resolution function. Led by this clue, we performed additional Levenberg–Marquardt fits to individual ND peaks using a superposition of two Gaussian profiles per peak: one with a width close to those in table 3, $W_i \approx 0.8°$, and another with a large W_i between 2° and 4°. Rather surprisingly, also these fits could explain the data to a precision of $\chi^2 \leqslant 1.7$. The analysis, using Scherrer's equation [44] as described at the end of section 3.2 individually for each fitted Gaussian profile, resulted in the following crude but statistically sufficient model: at $\mu_0 H = 0.0$ T, $12 \pm 2\%$ of the magnetic domains had a diameter of 20 ± 10 nm and the rest were of order 500 nm. At $\mu_0 H = 2.7$ T, on the other hand, all nanoscale domains had vanished and only domains of order 1000 nm remained. This was the conclusion both at $T = 55$ K and $T = 5$ K.

The actual distribution of magnetic domain sizes must naturally be broader than in our simplified two-component model, but it is clear that nanoscale domains are present in PCMO $x = 0.1$ near its ground state. It is noteworthy that we were not able to experimentally prepare the sample in a purely FM or AFM state, but only in a metastable mixture of both. In the context of manganites, the most probable explanation for the presence of such small domains is the the double-exchange-driven phase separation into FM and AFM clusters [3]. Our *ab initio* calculations also implicitly suggest a compatible instability of the A-AFM phase towards ferromagnetism, which could arguably be brought into manifestation by amplifying the double-exchange interaction using external stimuli [2–8, 10]. This provides an important piece of support for the model proposed to explain the photoinduced ferromagnetism in the material [7, 23]. That the phase separation description can be reasonably extended outside the 'optimal doping range' from $x = 0.3$ to $x = 0.5$ [3, 6, 8, 10] is an interesting and relatively novel observation as such, especially since no charge ordering (CO) is found to take place in PCMO $x = 0.1$ contrary to the other mentioned Ca concentrations.

The absence of long-range CO prevents PCMO $x = 0.1$ from undergoing a sudden metamagnetic AFM–FM insulator-to-metal transition like the one observed at $0.3 \leqslant x \leqslant 0.5$ [3, 10, 22, 49]. Indeed, the magnetic hysteresis loop of PCMO $x = 0.1$ is very regular at all temperatures below $T_C \approx 100$ K, with a soft ferromagnetic sigmoidal shape, modified only by a small linear component [22]. The linear component might be explained by the canting of magnetic Mn sublattices, but based on our present results, it is likely to originate at least partially from subtle shifts in the AFM–FM phase equilibrium. A comparison of the AC magnetic susceptibility data of PCMO at $0.0 \leqslant x \leqslant 0.5$ reveals that the relaxation time constant of the AFM–FM equilibrium system, assuming one is present, would actually be the lowest at $x = 0.1$, as seen by fits to the Vogel–Fulcher law [23, 51]. This is in agreement with our finding that each magnetic phase in PCMO $x = 0.1$ quickly forms internally well-ordered clusters which are large enough to diffract effectively, whereas the species of PCMO at larger x favour more frustrated spin glass phases [3, 23, 51]. The relaxation time is a sensitive function of the electronic carrier (hole) concentration in PCMO due to the dominance of the DE mechanism [23, 51].

Apart from the phase separation issue, our present study also revealed an ordered low-temperature Pr moment close to the full high-spin value of 2 μ_B per ion, which, surprisingly enough, is roughly 300% higher than earlier reports [1] propose. The convergence of our ND, SQUID and *ab initio* results leaves little doubt about the matter, however. The most important implications of this result may be in the context of the strong low-temperature magnetocaloric effect proposed in PCMO $x = 0.1$ [52, 53]. The FM ordering of the Pr magnetic moment is undoubtedly what stretches the relevant magnetic transition across such a wide temperature range (from ca. 150 K almost down to liquid He temperature), bringing up the refrigerant capacity estimate to its highest value within the PCMO family [53].

5. Conclusions

The low-temperature magnetostructure of PCMO $x = 0.1$ was revised using cold neutron powder diffraction (wavelengths 4.20 Å and 2.45 Å), SQUID magnetometry and *ab initio* computations. Previously published results [1, 24] of an A-AFM average ground state were reproduced to a good precision both experimentally and theoretically, and complemented by verifying that the effects of an applied magnetic field of 2.7 T on the magnetostructure could be approximately modeled within the same framework. However, in contrast to this simple and elegant model, explicit evidence of nanoscale magnetic clusters was obtained in the low-temperature ground state of PCMO $x = 0.1$ based on high resolution diffractograms. This finding was interpreted as an argument in favor of the recently proposed FM–AFM phase separation model used to explain a photoinduced ferromagnetism phenomenon in the material [7, 23]. We may conclude that the phase separation model is more physical than the canted AFM model [1, 24] since the explanatory power of the former matches and exceeds that of the latter. This point was particularly illuminated in the contexts of magnetic Rietveld analysis, the relative stabilites of *ab initio* solutions, magnetostriction and magnetic domain size distributions.

Based on a convergence of ND, SQUID and *ab initio* results, we also conclude that the low temperature magnetic moment of Pr must be 300% larger than previously thought, close to the high spin value of 2 μ_B per formula unit. This explains and supports the strong magnetocaloric entropy changes and high refrigerant capacities predicted in low-x PCMO below $T = 150$ K [52, 53].

Acknowledgments

This work is based on neutron scattering experiments performed at SINQ, Paul Scherrer Institute, Switzerland. The authors are thankful to Martin Hoffmann for his support concerning the Monte Carlo method. LU would like to thank DANSCATT for financial support. PP and JT wish to thank the Jenny and Antti Wihuri Foundation, Finland, for financial support. JT is also thankful for the resources provided by UTUGS. MG, WH and AE acknowledge support by the Deutsche Forschungsgemeinschaft through the Collaborative Research Center SFB 762 'Functionality of Oxide Interfaces' and by the Deutscher Akademischer Austauschdienst (DAAD).

References

[1] Jirák Z, Krupička S, Šimša Z, Dlouhá M and Vratislav S 1985 Neutron diffraction study of $Pr_{1-x}Ca_xMnO_3$ perovskites *J. Magn. Magn. Mater.* **53** 153–66

[2] Coey J M D, Viret M and von Molnár S 2009 Mixed-valence manganites *Adv. Phys.* **58** 571–697

[3] Dagotto E, Hotta T and Moreo A 2001 Colossal magnetoresistant materials: the key role of phase separation *Phys. Rep.* **344** 1–153

[4] Asamitsu A, Tomioka Y, Kuwahara H and Tokura Y 1997 Current switching of resistive states in magnetoresistive manganites *Nature* **388** 50–2

[5] Yoshizawa H, Kawano H, Tomioka Y and Tokura Y 1995 Neutron-diffraction study of the magnetic-field-induced metal-insulator transition in $Pr_{0.7}Ca_{0.3}MnO_3$ *Phys. Rev.* B **52** R13145–8

[6] Beaud P *et al* 2014 A time-dependent order parameter for ultrafast photoinduced phase transitions *Nat. Mater.* **13** 923–7

[7] Majumdar S, Elovaara T, Huhtinen H, Granroth S and Paturi P 2013 Crystal asymmetry and low-angle grain boundary governed persistent photoinduced magnetization in small bandwidth manganites *J. Appl. Phys.* **113** 063906

[8] Cox D E, Radaelli P G, Marezio M and Cheong S-W 1998 Structural changes, clustering, and photoinduced phase segregation in $Pr_{0.7}Ca_{0.3}MnO_3$ *Phys. Rev.* B **57** 3305–14

[9] Langner M C *et al* 2015 Ultrafast x-ray and optical signatures of phase competition and separation underlying the photoinduced metallic phase in $Pr_{1-x}Ca_xMnO_3$ *Phys. Rev.* B **92** 155148

[10] Elovaara T, Majumdar S, Huhtinen H and Paturi P 2015 Photoinduced colossal magnetoresistance under substantially reduced magnetic field *Adv. Funct. Mater.* **25** 5030–7

[11] Alonso J A, Martínez-Lope M J, Casais M T and Fernández-Díaz M T 2000 Evolution of the jahn-teller distortion of MnO_6 octahedra in $RMnO_3$ perovskites (R = Pr, Nd, Dy, Tb, Ho, Er, Y): a neutron diffraction study *Inorg. Chem.* **39** 917–23

[12] Kajimoto R, Mochizuki H, Yoshizawa H, Okamoto S and Ishihara S 2004 Ferromagnetic insulating phase in $Pr_{1-x}Ca_xMnO_3$ *Phys. Rev.* B **69** 054433

[13] Mercone S, Wahl A, Simon C and Martin C 2002 Nonlinear electrical response in a non-charge-ordered manganite: $Pr_{0.8}Ca_{0.2}MnO_3$ *Phys. Rev.* B **65** 214428

[14] Mercone S, Hardy V, Martin C, Simon C, Saurel D and Brûlet A 2003 Field dependence of the electronic phase separation in $Pr_{0.67}Ca_{0.33}MnO_3$ by small-angle magnetic neutron scattering *Phys. Rev.* B **68** 094422

[15] Frontera C, García-Muñoz J L, Llobet A, Respaud M, Broto J M, Lord J S and Planes A 2000 Phase coexistence, magnetic inhomogeneity, and disorder in the charge-ordered state of $Pr_{2/3}Ca_{1/3}MnO_3$ *Phys. Rev.* B **62** 3381–8

[16] Lees M R, Barratt J, Balakrishnan G, Paul D M and Ritter C 1998 Neutron-powder-diffraction study of the magnetic and structural properties of $Pr_{0.6}(Ca_{1-x}Sr_x)_{0.4}MnO_3 (0 \leqslant x \leqslant 1)$ *Phys. Rev.* B **58** 8694–703

[17] Respaud M, Llobet A, Frontera C, Ritter C, Broto J M, Rakoto H, Goiran M and García-Muñoz J L 2000 High magnetic field study of lattice and magnetic effects on the charge-melting transition in $L_{1/2}Ca_{1/2}MnO_3$ perovskites *Phys. Rev.* B **61** 9014–8

[18] Jirák Z, Martin C, Hervieu M and Hejtmánek J 2002 Charge and spin configurations in $Pr_{1-x}Ca_xMnO_3$ ($x = 0.5$–0.75) *Appl. Phys.* A **74** S1755–7

[19] Jirák Z, Damay F, Hervieu M, Martin C, Raveau B, André G and Bourée F 2000 Magnetism and charge ordering in $Pr_{0.5}Ca_xSr_{0.5-x}MnO_3$ ($x = 0.09$ and 0.5) *Phys. Rev.* B **61** 1181–8

[20] Jirák Z, Hadová E, Kaman O, Knížek K, Maryško M, Pollert E, Dlouhá M and Vratislav S 2010 Ferromagnetism versus charge ordering in the $Pr_{0.5}Ca_{0.5}MnO_3$ and $La_{0.5}Ca_{0.5}MnO_3$ nanocrystals *Phys. Rev.* B **81** 024403

[21] Rodríguez-Carvajal J, Daoud-Aladine A, Pinsard-Gaudart L, Fern M T and Revcolevschi A 2002 A new interpretation of the CO state in half-doped manganites: new results from neutron diffraction and synchrotron radiation experiments *Physica* B **320** 1–4 (Proc. of the 5th Latin American Workshop on Magnetism, Magnetic Materials and Their Applications)

[22] Elovaara T, Huhtinen H, Majumdar S and Paturi P 2012 Irreversible metamagnetic transition and magnetic memory in small-bandwidth manganite $Pr_{1-x}Ca_xMnO_3$ ($x = 0.0$–0.5) *J. Phys.: Condens. Matter* **24** 216002

[23] Elovaara T, Huhtinen H, Majumdar S and Paturi P 2014 Linear and nonlinear ac susceptibilities in polycrystalline low-bandwidth $Pr_{1-x}Ca_xMnO_3$ ($x = 0.0$–0.3) manganite *J. Phys.: Condens. Matter* **26** 266005

[24] Jirák Z, Vratislav S and Zajíček J 1979 The magnetic structure of $Pr_{0.9}Ca_{0.1}MnO_3$ *Phys. Status Solidi* A **52** K39–K43

[25] Rodríguez-Carvajal J 1993 Recent advances in magnetic structure determination by neutron powder diffraction *Physica* B **192** 55–69

[26] Ebert H, Ködderitzsch D and Minár J 2011 Calculating condensed matter properties using the KKR-Green's function method—recent developments and applications *Rep. Prog. Phys.* **74** 096501

[27] Hohenberg P and Kohn W 1964 Inhomogeneous electron gas *Phys. Rev.* **136** B864–71

[28] Kohn W and Sham L J 1965 Self-consistent equations including exchange and correlation effects *Phys. Rev.* **140** A1133–8

[29] Takeda T 1978 The scalar relativistic approximation *Z. Phys.* B **32** 43–8

[30] Koelling D D and Harmon B N 1977 A technique for relativistic spin-polarised calculations *J. Phys. C: Solid State Phys.* **10** 3107

[31] Marques M A L, Oliveira M J T and Burnus T 2012 Libxc: a library of exchange and correlation functionals for density functional theory *Comput. Phys. Commun.* **183** 2272–81

[32] Perdew J P, Ruzsinszky A, Csonka G I, Vydrov O A, Scuseria G E, Constantin L A, Zhou X and Burke K 2008 Restoring the density-gradient expansion for exchange in solids and surfaces *Phys. Rev. Lett.* **100** 136406

[33] Gyorffy B L 1972 Coherent-potential approximation for a nonoverlapping-muffin-tin-potential model of random substitutional Alloys *Phys. Rev.* B **5** 2382–4

[34] Temmerman W M, Gyorffy B L and Stocks G M 1978 The atomic sphere approximation to the KKR-CPA: electronic structure of paramagnetic Cu_cNi_{1-c} alloys *J. Phys. F: Met. Phys.* **8** 2461
[35] Faulkner J S and Stocks G M 1980 Calculating properties with the coherent-potential approximation *Phys. Rev.* B **21** 3222–44
[36] Anisimov V I, Zaanen J and Andersen O K 1991 Band theory and Mott insulators: hubbard U instead of Stoner I *Phys. Rev.* B **44** 943–54
[37] Liechtenstein A I, Katsnelson M I, Antropov V P and Gubanov V A 1987 Local spin density functional approach to the theory of exchange interactions in ferromagnetic metals and alloys *J. Magn. Magn. Mater.* **67** 65–74
[38] Krupička S, Maryško M, Jirák Z and Hejtmánek J 1999 Details of structural and magnetic transitions in $Pr_{0.5}Ca_{0.5-x}Sr_xMnO_3$ perovskites *J. Magn. Magn. Mater.* **206** 45–67
[39] Maryško M and Jirák Z 2008 Magnetization Study of the AFM-FM Coexistence in the Manganite System $Pr_{0.5}Ca_{0.5-x}Sr_xMnO_3$ *Acta Phys. Pol.* A **113** 143–6
[40] Higuchi T, Yajima T, Fitting Kourkoutis L, Hikita Y and Nakagawa N 2009 Mn_3O_4 precipitates in laser-ablated manganite films *Appl. Phys. Lett.* **95** 043112
[41] Song G B, Amaral J S, Amaral V S and Kholkin A L 2007 Processing and phase separation of LSMO-based multiferroic composite ceramics *J. Eur. Ceram. Soc.* **27** 3941–5
[42] Si P Z, Li D, Choi C J, Li Y B, Geng D Y and Zhang Z D 2007 Large coercivity and small exchange bias in Mn_3O_4/MnO nanoparticles *Solid State Commun.* **142** 723–26
[43] David W I F 2004 Powder diffraction: least-squares and beyond *J. Res. Natl Inst. Stand. Technol.* **109** 107–23
[44] Patterson A L 1939 The scherrer formula for x-ray particle size determination *Phys. Rev.* **56** 978–82
[45] Tokura Y and Tomioka Y 1999 Colossal magnetoresistive manganites *J. Magn. Magn. Mater.* **200** 1–23
[46] Pollert E, Krupička S and Kuzmičová E 1982 Structural study of $Pr_{1-x}Ca_xMnO_3$ and $Y_{1-x}Ca_xMnO_3$ perovskites *J. Phys. Chem. Solids* **43** 1137–45
[47] Marquardt D W 1963 An algorithm for least-squares estimation of nonlinear parameters *J. Soc. Ind. Appl. Math.* **11** 431–41
[48] Koon N C, Williams C M and Das B N 1991 Giant magnetostriction materials *J. Magn. Magn. Mater.* **100** 173–85
[49] Tokunaga M, Miura N, Tomioka Y and Tokura Y 1998 High-magnetic-field study of the phase transitions of $R_{1-x}Ca_xMnO_3$ (R = Pr, Nd) *Phys. Rev.* B **57** 5259–64
[50] Demin R V, Koroleva L I and Mukovskii Y M 2005 Giant volume magnetostriction and colossal magnetoresistance at room temperature in $La_{0.7}Ba_{0.3}MnO_3$ *J. Phys.: Condens. Matter* **17** 221–6
[51] Elovaara T, Huhtinen H, Majumdar S and Paturi P 2014 Study of dynamic magnetism in low bandwidth manganite $Pr_{1-x}Ca_xMnO_3$ (x = 0.3–0.5) by ac susceptibility measurements *J. Low Temp. Phys.* **175** 554–63
[52] Reis M S, Amaral V S, Araújo J P, Tavares P B, Gomes A M and Oliveira I S 2005 Magnetic entropy change of $Pr_{1-x}Ca_xMnO_3$ manganites ($0.2 \leqslant x \leqslant 0.95$) *Phys. Rev.* B **71** 144413
[53] Tikkanen J, Huhtinen H and Paturi P 2014 The magnetocaloric performance of (Pr,Ca) manganites estimated by magnetic transition entropies *IEEE Trans. Magn.* **50** 1–4